Aging Behaviors of Organic Electrophoretic Coating on Magnesium Alloy

Xiaoxue Wang [1,2], Guohui Wang [3], Yuan Jing [3], Kai Zheng [3], Rongqiao Wang [1], Xiuchun Liu [2], Kai Gao [2], Jingli Sun [4], Yong Yuan [4] and Fandi Meng [3,*]

1   School of Energy and Power Engineering, Beihang University, Beijing 100191, China; wangxx@buaa.edu.cn (X.W.); wangrq@buaa.edu.cn (R.W.)
2   Beijing Institute of Space Long March Vehicle, Beijing 100076, China; liuxc@163.com (X.L.); gaok@163.com (K.G.)
3   The School of Materials Science and Engineering, Northeastern University, Shenyang 110819, China; wanggh8221029@163.com (G.W.); jingyuan@mail.neu.edu.cn (Y.J.); zkd240157021@163.com (K.Z.)
4   Shanghai Spaceflight Precision Machinery Institute, Shanghai 201600, China; sunjingli@163.com (J.S.); yuanyong@163.com (Y.Y.)
*   Correspondence: fandimeng@mail.neu.edu.cn

Abstract: VW63Z magnesium alloy, known for its high strength-to-weight ratio and excellent mechanical properties, is a promising candidate for applications in the automotive industries. Among the anti-corrosion technologies for VW63Z alloys, organic electrophoretic coatings have gained significant attention due to their ability to provide a uniform and controlled coating thickness, high coating adhesion, and excellent corrosion protection properties. In this work, to investigate the aging behaviors of an organic electrophoretic coating for magnesium alloys, water absorption kinetics curves of the coatings after immersion in 3.5 wt.% NaCl at 20 °C and 40 °C were measured, and parameters such as the saturated water absorption and saturation time of the free film coatings were fitted to determine the densification evolution of the organic coatings. A tensile test was used to test the tensile strength of the organic coating during service to determine the evolution of the strength and toughness of the organic coating. The evolution of wet adhesion of organic coatings with service time was tested by ASTM D4541-02. The impedance spectra of the organic coatings under the above conditions were detected by EIS, and finally, the failure behavior of the organic coatings under immersion was analyzed.

Keywords: electrophoretic coating; aging behavior; water absorption; magnesium alloy

1. Introduction

Magnesium alloys are known for their low weight and high strength-to-weight ratio, making them attractive materials for various industrial applications [1–3]. In the automotive industries, weight reduction is paramount for improving fuel efficiency and reducing emissions. Moreover, the complex component manufacturing, including engine blocks, transmission cases, and structural frames, puts high demands on the machinability and castability of the materials [4,5]. VW63Z magnesium alloy is a promising candidate for automotive industries applications due to its lightweight nature and excellent machinability [6,7]. However, one of the challenges associated with VW63Z is its susceptibility to corrosion, which can significantly affect its long-term performance and durability [8–10]. To address this issue, various surface treatment methods have been developed to protect magnesium alloys from corrosion and improve their overall performance [11–14]. One such method is the application of organic coatings, which serve as a barrier against corrosive environments and provide additional benefits such as improved adhesion and aesthetics.

Organic coatings for magnesium alloys typically consist of a binder polymer matrix loaded with corrosion inhibitors and other functional additives [15,16]. These coatings

can be applied through a variety of methods, including spraying, dip coating, and electrophoretic deposition [17–19]. Among these methods, organic electrophoretic coating has gained significant attention due to its ability to provide a uniform and controlled coating thickness, high coating adhesion, and excellent corrosion protection properties [20–23]. The electrophoretic coating process involves applying an electric field to attract charged particles suspended in a liquid dispersion toward the magnesium alloy substrate, resulting in a tightly adhered and protective coating layer. Electrophoretic coating is considered an environmentally friendly process as it generates minimal hazardous waste. This aligns with the automotive industry's growing emphasis on sustainability and reducing environmental impacts. Therefore, the electrophoretic coating of magnesium alloys represents a promising approach to overcoming the limitations associated with their corrosion susceptibility.

The aging behaviors of organic electrophoretic coatings for magnesium alloys have been the subject of extensive research in recent years [6,24–34], including the application of anti-corrosion [35,36], bioactive [37,38], anti-microbial [26,39], and anti-wear coatings [40,41], among others [42,43] described; understanding the long-term performance and durability of these coatings is crucial for ensuring the reliability and longevity of magnesium alloy-based components. Ghasemi et al. [40] improved the electrophoretic coating by graphene oxide (GO) and conducted hardness tests, drop contact angle tests, and EIS tests. The results show that an addition of 2 wt.% GO can significantly improve the mechanical properties of coatings, mainly due to the bridging effect of GO nanosheets between the alumina nanoparticles. Gnedenkov et al. [44] modified polymer-containing coatings with super dispersed polytetrafluoroethylene to control the alloy resorption kinetics, resulting in a suitable Mg alloy biodegradation. The addition of bioactive hydroxyapatite (HA) in the electrophoretic coating is widely studied due to the application prospects of magnesium alloys in the biomedical field [45]. Potentiodynamic polarization (PDP) studies have shown that Mg-6Zn-0.5Zr alloy coated with a 15 μm thick HA-coating decreased the degradation rate by approximately four times in Ringer's solution [46]. Aging phenomena such as water absorption, corrosion resistance, adhesion strength, and mechanical properties can be influenced by factors such as exposure to environmental conditions and temperature fluctuations [47]. By investigating the effects of aging on coatings, strategies to improve the sustainability and performance of magnesium alloy systems in various applications can be developed [48–51]. N. Guermazi et al. [52] studied the sorption kinetics of coatings through the water absorption rate response at different temperatures. A decrease in the mechanical properties, including the elastic modulus and tensile strength, was clearly observed. This also shows that such degradation largely depends on both the aging temperature and immersion duration. A. Lopez-Ortega et al. [53] evaluated three coatings employed for offshore component protection according to certain standards by performing weathering aging tests in different climatic cabinets. However, the aging process of thin electrophoretic coatings on magnesium alloys has rarely been reported.

The aim of this study is to promote an understanding of the failure behavior and durability of the organic electrophoretic coatings, which can provide some experimental guidance for failure analysis in practical applications and even for the research of coating lifetime predictions. To investigate the aging behavior of an organic electrophoretic coating on magnesium alloys, water absorption kinetics curves of the coatings after immersion in 3.5 wt.% NaCl at 20 °C and 40 °C were measured, and parameters such as the saturated water absorption and saturation time of the free film coatings were fitted to determine the densification evolution of the organic coatings. A tensile test was used to test the tensile strength and fracture elongation of the organic coating during service to determine the evolution of the strength and toughness of the organic coating. The evolution of wet adhesion of organic coatings with service time was tested by ASTM D4541-02. The impedance spectra of the organic coatings under the above conditions were detected by EIS, and finally, the failure behavior of the organic electrophoretic coatings under immersion was analyzed.

2. Materials and Methods

2.1. Experimental Materials

The substrate is an as-cast VW63Z magnesium alloy provided by Shenyang Zhongjie Metals Co., Ltd. (Shenyang, China), with a size of 40 mm × 40 mm × 5 mm. The chemical composition was analyzed by ICP-OES (inductively coupled plasma—optical emission spectroscopy, ULTIMA 2, Horiba Scientific, Kyoto, Japan), and the results are listed as follows in mass percentiles: Gd 5.63, Y 2.73, Zr 0.37, Fe 0.10, Mn 0.14, Si 0.10, Al 0.09 and Mg the balance. The pre-treatments included polishing, degreasing (10.0 g/L NaOH, 5.0 g/L Na_2CO_3, and 8.0 g/L $Na_2O \cdot nSiO_2$), water washing, rust removal (10 g/L HCl and 18 g/L HF), and phosphating.

The electrophoresis coating was prepared using a Nippon E-coating paint (Nippon Paint Holdings Co., Ltd., Osaka, Japan) containing a soluble metal compound, amine-modified resin, and curing agent. The electrophoresis coating equipment is an HD-EDC-1000 from Huada, Beijing, China. The set-up of the electrophoresis coating system is shown in Figure 1. The process parameters were as follows: 100 V voltage for 10 min, a bath temperature of 25~30 °C, and a curing temperature of 200 °C for 10 h. The produced samples with defects such as holes and bubbles were screened out by visual inspection of the coating surface. The surface micromorphology of intact coatings by SEM (EM-30AX, COXEM, Daejeon, Korea) is shown in Figure 2a. It can be seen that the coating surface is relatively smooth, with almost no visible defects such as pores. The free film was obtained by dissolving the base metal. Finally, a PosiTector 6000 Coating Thickness Gauge manufactured by Delelsko Corporation (Ogdensburg, NY, USA) was utilized to measure the thickness of the coating at various points in different areas of the coating to ensure that all coating/metal specimens used in the experiments had a coating thickness of 30 ± 2 μm. The coating thickness can also be obtained through a cross-sectional morphology image (Figure 2b), and its values are in good agreement with the results from the thickness gauge.
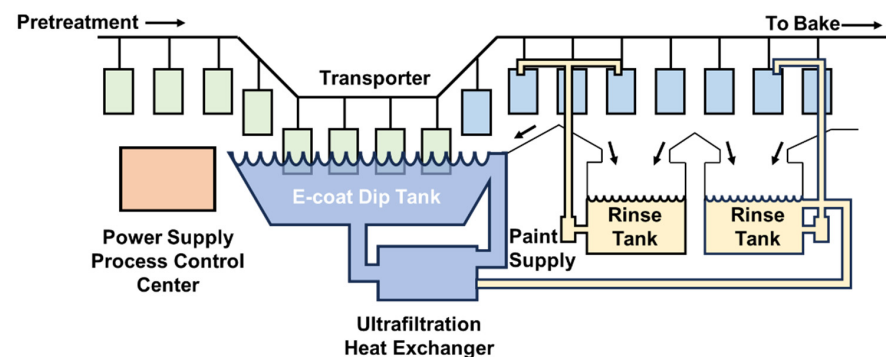

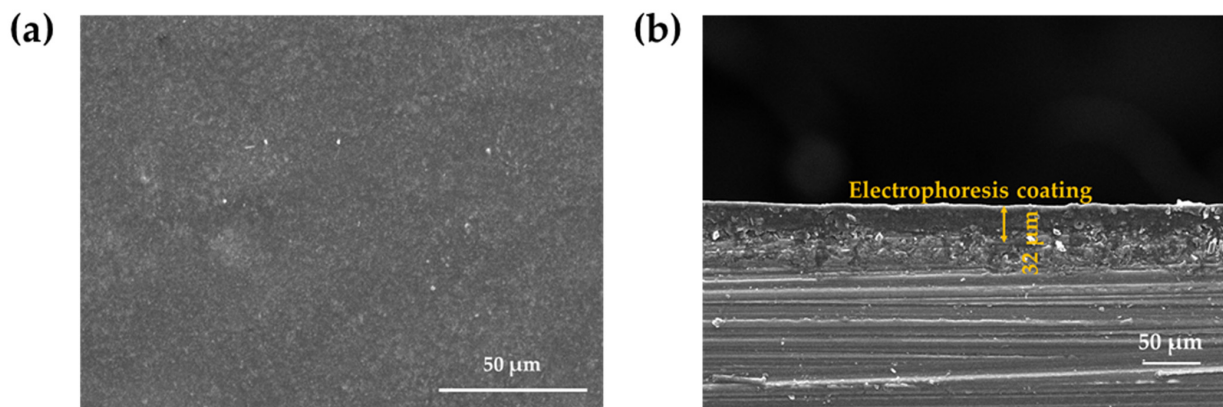**Figure 1.** Schematic diagram of the electrophoresis coating system.

Figure 2. (**a**) Typical SEM micromorphology of the surface of the intact electrophoretic coating and (**b**) cross-section micromorphology of the coating/alloy system.

2.2. Experimental Methods

2.2.1. Tensile Tests

The tensile tests of the electrophoretic coatings were evaluated by a universal tensile testing machine (AK20KN, Shimadzu, Kyoto, Japan) with a strain rate of 2 mm/min, according to ISO 37-2005.

2.2.2. Gravimetric Test

Gravimetric data were obtained by measuring the mass of the electrophoretic coatings at stipulated time intervals at different temperatures. Before weighing, the surface was carefully cleaned with filter paper, and a Sartorius (Göttingen, Germany) BS124S microbalance (1 μg resolution) was used as the weighing device. The experiment was performed three times to ensure reproducible results. The water absorption (Q_t) was then calculated according to the following equation:

$$Q_t = \frac{m_t - m_0}{m_0} \times 100\% \tag{1}$$

where m_t represents the mass of electrophoretic coatings at time t, m_0 is the initial mass before immersion, and Q_t is the water absorption (mass%) at time t.

2.2.3. Adhesion Tests

The adhesion tests were carried out according to ASTM D4541-09. This test was performed with a PosiTest manual hydraulic pull-off adhesion tester from DeFelsko, Ogdensburg, NY, USA. At least 5 parallel samples were taken, and the average value was taken as the final result.

2.2.4. EIS Tests

EIS tests of the intact and scratched coatings were performed in 3.5 wt.% NaCl solution using an electrochemical workstation (PARSTAT 4000 A). For the electrophoretic coatings, a traditional three-electrode system was used, in which a platinum sheet, a saturated calomel electrode, and a coated Mg alloy with an exposed area of 4 cm^2 were used as auxiliary, reference, and working electrodes, respectively. The working electrode was held at its open circuit potential (OCP) for 1200 s prior to the measurement to ensure that the OCP reached a steady state. EIS tests were performed over a frequency range of 0.01 Hz to 10^5 Hz with alternating current signal amplitudes of 20~50 mV, and all EIS data were fitted by ZSimpWin software V3.50.

3. Results

3.1. Gravimetric Results for Electrophoretic Coatings

By means of weight testing, the mass of absorbed water in the free film can be calculated to study in detail the water absorption behavior of the coating. As shown in Figure 3, the corresponding water absorption kinetic curves at both temperatures indicate that the water transport in the electrophoretic layer can be divided into three stages: the absorption stage, saturation stage, and decline stage. In Figure 3a, a quick growing trend of water absorption was observed in the initial period of the curve at 20 °C. This suggested that water diffused rapidly through the microscopic channels in the coating. Then, the value of immersion at 20 °C gradually reached saturation at approximately 1080 h. In the saturation stage, the water absorption rate of the coating tends to stabilize with a certain fluctuation phenomenon. The absorption stage and saturation stage of the curve follow Fick's law of diffusion. The saturation water absorption rate was determined to be approximately 0.94% at 20 °C. Subsequently, there is a certain decrease in water absorption, which may be caused by the dissolution of substances due to the degradation of the coating.
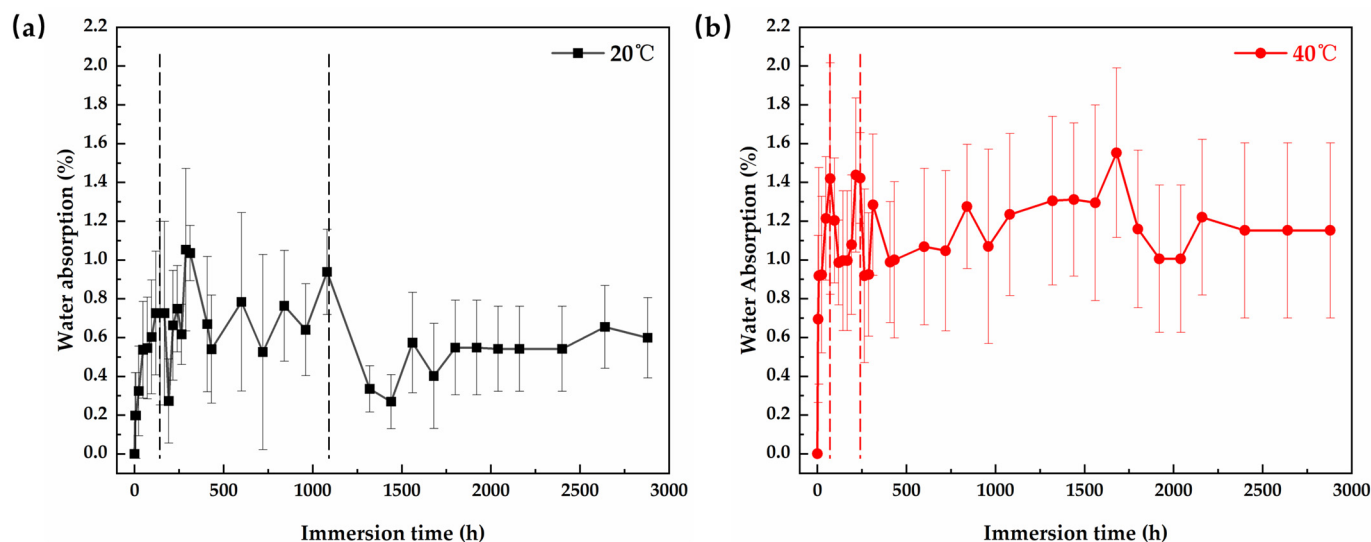
Figure 3. Water absorption curves for the coatings at (**a**) 20 °C and (**b**) 40 °C.

On the other hand, the curve of immersion at 40 °C also involved these three stages (Figure 3b). The curve reaches saturation after approximately 228 h. The saturation water absorption rate was determined to be approximately 1.42% at 40 °C. From the results above, it can be seen that the saturated water absorption at 40 °C is greater than that at 20 °C, and the time to reach saturation is more rapid. This indicates that an increase in temperature not only accelerates water transport but also increases the saturated water absorption rate of the coating. The water uptake in the coating is significantly promoted by the rise of temperature.

3.2. Adhesion Test Results for Electrophoretic Coatings

Figure 4a shows the variation in the adhesion of the coatings with the immersion period. Before immersion, the dry adhesion value was approximately 16.40 MPa. As we know, the dry adhesion will change to be wet adhesion after immersion in the water. With prolonged immersion, the values of the coatings at both temperatures decreased, indicating that the coating adhesion gradually decreased. In the initial period of immersion (before 100 h), the declines in coating adhesion were limited for both temperatures, which suggests that the coatings still retain a certain degree of protection capability. The coatings were pulled off to compare the adhesion profiles with each other (Figure 4b,d). It can be seen that the fracture pattern was a cohesive fracture after the pull-off tests. The morphology of fracture surfaces of the samples indicates that the coating adhesion is still good. After 336 h of immersion, the wet adhesion of the coatings immersed at 20 °C and 40 °C decreased to 6.44 ± 0.41 MPa and 5.41 ± 1.59 MPa, respectively. At the same time, the exposed areas of the substrate increase after pull-off tests (Figure 4c,e), suggesting a significant decrease in coating adhesion. However, the wet adhesion of the coating immersed at 40 °C dropped more than that immersed at 20 °C. The results above demonstrate that an increase in temperature accelerates the loss of coating adhesion.

3.3. Tensile Test Results for Electrophoretic Coatings

Mechanical property degradation severely affects the service life of the coating and induces failure of the protective performance, which is indispensable to know in research on coating failure behavior. For this purpose, tensile tests were performed on the electrophoretic free film to assess its mechanical properties, such as strength and toughness. Figure 5 shows some typical time-dependent load-displacement curves of the electrophoretic free films at 20 °C and 40 °C. During tensile deformation, the coating first undergoes the elastic deformation stage, with linear effects on the load and displacement. At this point, polymer deformation dominates the changes in the bond distance and bond

angle of the polymer chain. As the stress of the coating reaches the maximum yield strength, the stress is reduced until the coating fractures. For the coating, strain softening does not occur before fracture, which means that the overall mechanical properties of the coating are hard and brittle in this stage. In addition, the maximum load of the coating decreases at the expense of immersion at both temperatures. This phenomenon can be attributed to the hydrolysis between water molecules and the coating, which enables changes in the molecular bonds within the coating and further decreases the strength.
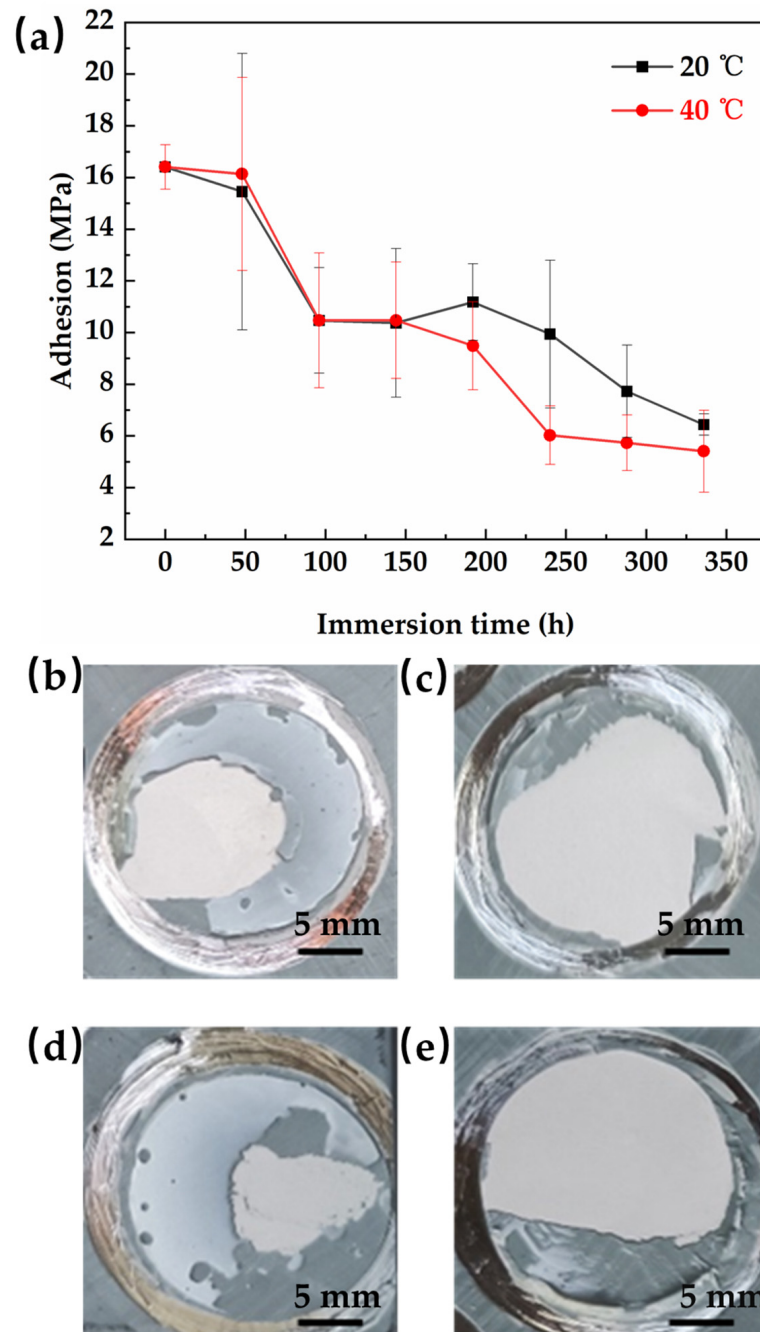

Figure 4. (**a**) Adhesion test results of electrophoretic coatings measured by the pull-off method at 20 °C and 40 °C, and the typical macroscopic morphology of fracture surfaces of the samples after pull-off tests: (**b**) immersed at 20 °C after 96 h, (**c**) immersed at 20 °C after 336 h, (**d**) immersed at 40 °C after 96 h, and (**e**) immersed at 40 °C after 336 h.

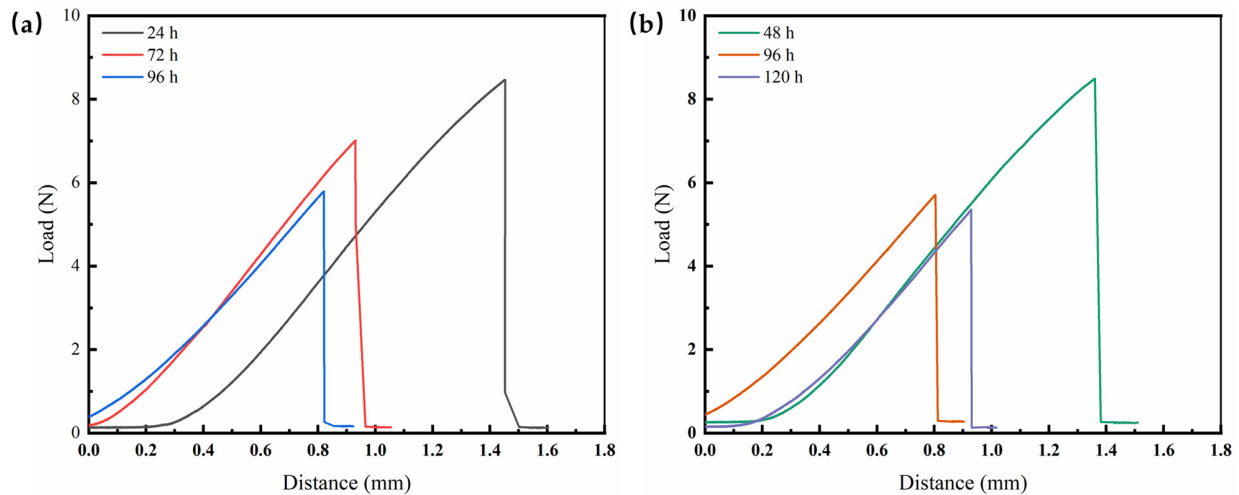**Figure 5.** (**a**) Typical tensile curves of electrophoretic coatings at 20 °C; (**b**) typical tensile curves of electrophoretic coatings at 40 °C.

Figure 6 intuitively shows the time-dependent variation in the tensile strength (σ) of the coating. The tensile strength of the free films at 20 °C and 40 °C decreased gradually. However, the downward trends have been accompanied by violent fluctuations, reflecting the large differences among the individual samples. In spite of this, the σ values decrease more slowly at 20 °C than at 40 °C on the whole. It is clear that the mechanical properties of the coating deteriorate quickly as the temperature increases.
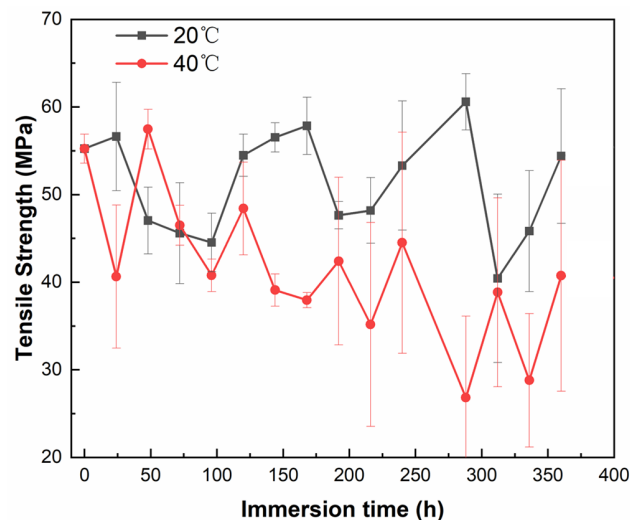

Figure 6. The statistical curves of the tensile strength for the electrophoretic free films at two temperatures.

3.4. EIS Results

Electrochemical impedance spectroscopy (EIS) can reflect information regarding coating deterioration and metal corrosion, and the variation in coating failure can be determined through in situ monitoring of coating/metal electrodes. The resulting data can provide a benchmark for the protective performance of the coating. Figure 7 shows the Nyquist and Bode plots of the sample immersed at 20 °C for different immersion times. The Nyquist plot exhibits a single capacitance resistance arc at the beginning, and the low-frequency impedance modulus ($|Z|_{0.01Hz}$) can reach almost 10^{10} Ω cm^2. At this point, the corrosive media have not yet infiltrated into the surface of the metal substrate. The relevant equivalent electrical circuit (EEC) is depicted in Figure 7c. To accurately fit the impedance data, an EEC model incorporating a single time constant is employed. This model comprises the solution resistance (R_s), the coating capacitance (C_c), and the coating resistance (R_c). Due

to the "scattering effect" resulting from the heterogeneity of the coating surface, a constant phase element (CPE) has been utilized in place of the traditional capacitance element [54]. It was found that the impedance modulus of the coating dropped significantly after 1 day, dropping to the order of 10^8 $\Omega\cdot\text{cm}^2$, indicating that the corrosive medium began to enter the coating through the defect, resulting in a decline in the impedance modulus, as shown in Figure 7a. At the same time, a second arc of capacitive reactance appears in the Nyquist diagram of the coating, that is, the aging behavior entered the middle stage of immersion. When water is transferred to the coating/metal interface, electrochemical reactions begin to occur due to the establishment of corrosion cells. At this time, EIS features of two time constants began to appear on the coating (Figure 7b). The corresponding EEC (refer to Figure 7d) is employed, incorporating the double-layer capacitance (Q_{dl}) and the charge transfer resistance (R_{ct}) to achieve a precise fit with the experimental data. The impedance magnitude gradually decreased over immersion time. After 28 d of immersion, the $|Z|_{0.01\,\text{Hz}}$ value of the coating dropped to the order of 10^7 $\Omega\cdot\text{cm}^2$, indicating a bad corrosion protection of the coating.
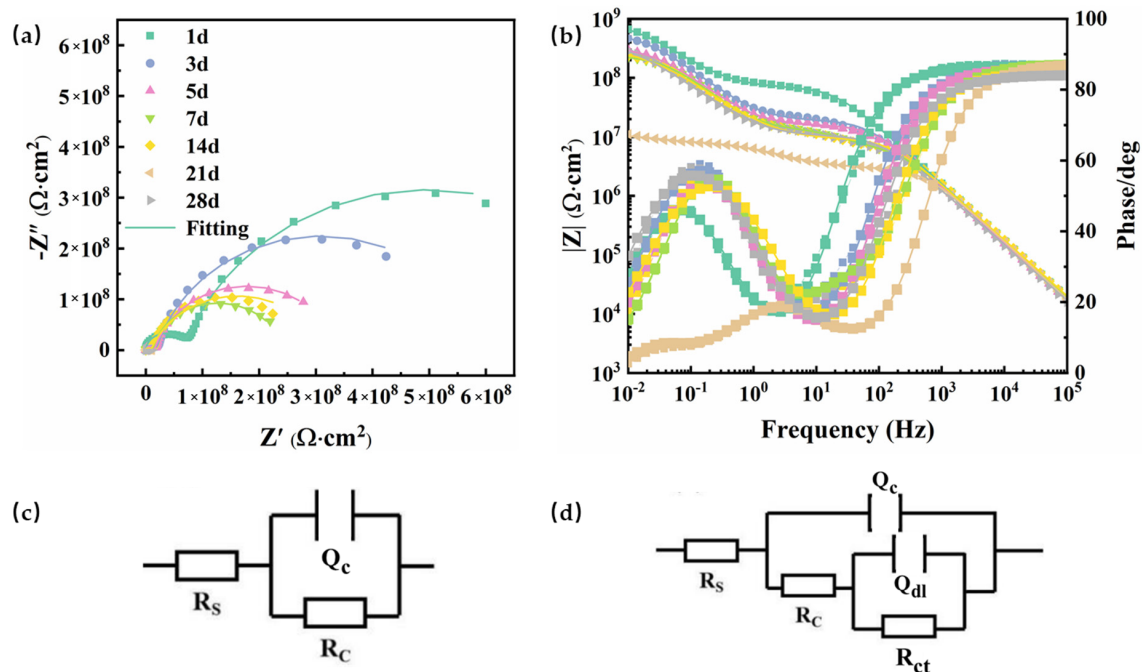

Figure 7. (**a**) Time-dependent Nyquist and (**b**) Bode plots of the coating immersed at 20 °C; (**c**) the corresponding EEC with a single time constant and (**d**) EEC with two time constants.

In Figure 8, it can be seen that the whole failure behavior of the coating immersed at 40 °C has not much of a difference from that at 20 °C. The $|Z|_{0.01\,\text{Hz}}$ value of the coating sharply decreased to 10^8 $\Omega\cdot\text{cm}^2$. After immersion for 14 d, the impedance modulus was 10^7 $\Omega\cdot\text{cm}^2$, which means that the coating lost its barrier function against electrolyte permeation. According to the results, the aging process of the coating was accelerated by an increase of temperature, resulting in a decline in the impedance modulus. As for the phenomenon of a temporary rising trend of the impedance modulus after 21 days, it can be inferred that the impedance modulus of the coating/metal corrosion interface increased with the accumulation of corrosion products.

3.5. SEM Micrographs and EDS Results of the Coatings after Immersion

Since there is no essential difference in the failure characteristics of the micro morphology of the coating after immersion at 20 °C and 40 °C, the SEM surface micrographs of the coating after 21 days of immersion at 40 °C are taken as a representative result. In Figure 9a, an obvious pore can be found in the surface of the coating, which is different from the

morphology of coating before immersion (see Figure 2a). The localized magnified image of the hole edge shows the presence of substances resembling corrosion products (Figure 9b). In order to analyze the possible causes of the surface hole formation, EDS analysis was performed sequentially from near to far distances from the hole edge (Figure 9c–e). It can be seen that a large amount of Mg, O, and some trace elements from the matrix metal were detected, suggesting the formation of significant corrosion products at the edges of the pits (Figure 9c). As the distance from the pits increases, the content of elements from the metallic matrix significantly decreases (Figure 9d). At the farthest position (Position III in Figure 9b), the detected elements originate from the coating (Figure 9e), indicating that no corrosion products were found further away from the pits. It can be reasonably inferred that the corrosion media penetrate through the coating and cause substrate corrosion, leading to the accumulation of corrosion products. The gradually accumulating corrosion products and generated gases on the alloy surface pushed the coating until it cracked, leading to the formation of a pore and a decrease in coating adhesion [15,24,55,56]. Compared to the protective performance of the coating before immersion, it significantly declined to a very low level at this stage, which is consistent with the results shown by the EIS.
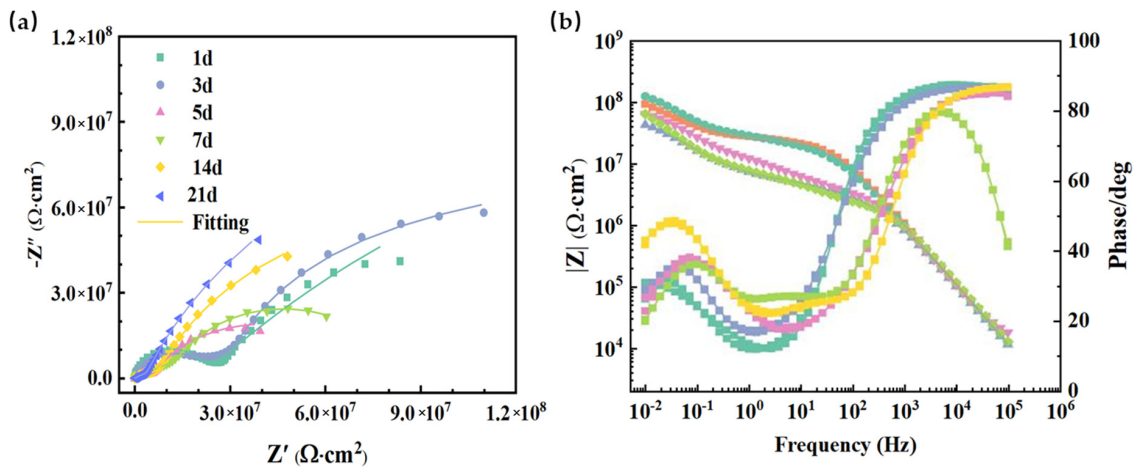

Figure 8. (**a**) Time-dependent Nyquist and (**b**) Bode plots of the coating immersed at 40 °C.
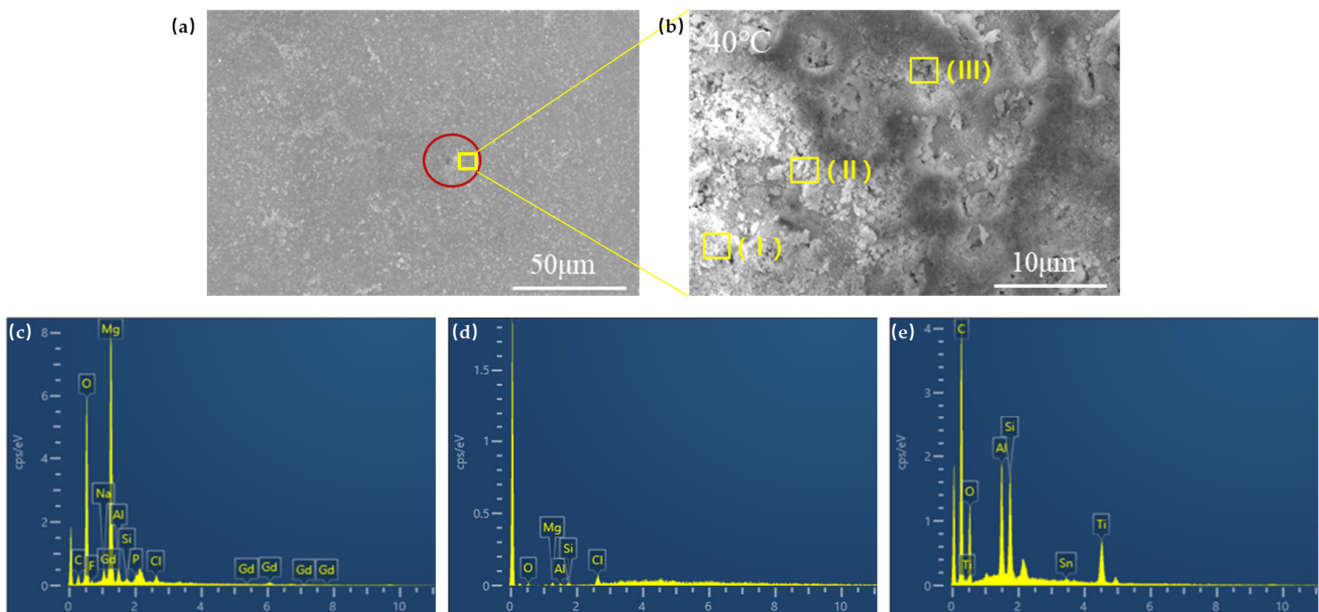

Figure 9. (**a**) SEM micrographs of the coating surface after 21 days of immersion at 40 °C and (**b**) localized magnified image of the hole edge of the coating; (**c**–**e**) EDS results of the coating surface at the positions of I, II, and III.

4. Discussion

4.1. Water Transport Behavior

To describe the moisture absorption behavior of the coating, a theoretical diffusion model of the coating was established for one-dimensional moisture transport. Based on Fick's diffusion law, the theoretical diffusion mathematical model of coating under a normal pressure aqueous solution is shown as follows:

$$\frac{\partial c(x,t)}{\partial t} = D \frac{\partial^2 c(x,t)}{\partial x^2} \tag{2}$$

where $c(x,t)$ is the solution concentration; x is the distance from the coating surface; t is immersion time; and D is the diffusion coefficient. The model holds that water obeys Fick's second diffusion law in the initial stage of coating transport, and its typical absorption diffusion equation is as follows [57,58]:

$$\frac{Q_t}{Q_\infty} = 1 - \frac{8}{\pi^2} \sum_{n=0}^{\infty} \frac{1}{(2n+1)^2} \exp\left[\frac{-(2n+1)^2 D\pi^2}{d^2} t\right] \tag{3}$$

where Q_t and Q_∞ represent the adsorbed water weight of the penetrant at time t and after saturation, respectively; d is the thickness of the test sample.

This equation is an ideal case of penetrant transport in polymers, which corresponds to the free diffusion of penetrant without the interference of polymer chain rearrangement or external influence. For relatively small values of t, Equation (3) can be simplified to Equation (4):

$$\frac{Q_t}{Q_\infty} = \frac{2\sqrt{D}}{d\sqrt{\pi}} \sqrt{t} \tag{4}$$

Assuming that the coating is saturated at time t, then $Q_t/Q_\infty = 1$. Substituting the parameters of the saturation absorption time (t) and the thickness of the coating (d) into Equation (4), the diffusion coefficient D_{20} is $1.817 \times 10^{-16}/m^2\ s^{-1}$ at 20 °C, and D_{40} is $8.610 \times 10^{-16}/m^2\ s^{-1}$ at 40 °C.

According to Equation (4), when the coating diffusion coefficient D and the saturated water absorption Q_∞ are given (see Table 1), the time t required to reach the amount of water absorption is

$$t = \left(\frac{Q_t}{Q_\infty}\right)^2 \frac{d^2 \pi}{4D} \tag{5}$$

The resulting model equation for the water transport behavior of the electrophoretic coatings at both temperatures is

$$t_{20°C} = 1.094 \times 10^9 Q_t^2 \tag{6}$$

$$t_{40°C} = 1.746 \times 10^8 Q_t^2 \tag{7}$$

In summary, the results testify that a high temperature obviously accelerates the water diffusion through the coating. It is observed that although the change of temperature has a great influence on the diffusion coefficient, the diffusion behavior of the coating does not change essentially.

Table 1. The data are related to the diffusion of the coating at 20 °C and 40 °C.

Conditions	d/mm	t/h	Q_∞/g	D/m^2 s^{-1}
20 °C	0.03	1080	0.05816	1.817×10^{-16}
40 °C	0.03	228	0.06853	8.610×10^{-16}

4.2. Coating Adhesion Modeling

The bonding force of organic coatings with magnesium alloys is highly dependent on the service environment. As mentioned above, the wet-state adhesion of coatings with immersion time exhibits a nonlinear change under different temperatures. If the adhesion fails, the other protection process will become useless. However, the complex influencing factors make the study of wet adhesion difficult, and there is an urgent need to employ mathematical models or predictive equations to explore the underlying mechanisms.

According to our previous research, gray system theory (GST) is a superior method for studying wet-adhesion models [59]. Among the numerous available information processing and mathematical model analysis methods, gray system theory is famous for its intrinsic characteristics, namely that it has few data requirements and can explore potential mechanisms with little information. Gray system theory was proposed by Deng Julong and can reveal the evolutionary pattern of things in the context of a small number of excavations and little information [60]. The core of the gray system theoretical model is the gray dynamic model, or the GM model for short. The most typical model is the GM (1, 1) gray model.

In this study, the adhesion between the organic coating and the substrate was affected by many factors, which, in addition to the service environment of the coating, was related to the preparation and curing process and material structure. Given that the connotation of the change in coating adhesion is unclear but the extension is clear, it is necessary to choose appropriate mathematical methods for modeling. Based on the concept of the gray generation function, with differential fitting as the core, the essence of gray system theory is that all random quantities are gray quantities and gray processes that change within a certain range and within a certain period of time. The purpose of gray quantity processing is not to determine the statistical pattern and probability distribution but rather to turn the original data series into regular time series data through certain methods; that is, the pattern of finding the number by the number is established. The GM (α, β) model is the core of gray prediction, where α is the order of the differential equation and β is the number of variables. Among them, the GM (1, 1) model, which consists of a first-order differential equation and one variable, is considered to be the most widely used gray prediction model due to the small amount of raw information, the simplicity of the calculation method, and the high accuracy of the model. As a result, the variation rule of wet adhesion of the organic coating was established through the gray GM (1, 1) model, and the specific process was as follows:

The sequence $X^{(0)}$, which denotes the wet adhesion of a coating/metal substrate system at different immersion times, is defined as follows:

$$\left\{ X^{(0)} \right\} = \left\{ X^{(0)}{}_{(1)}, X^{(0)}{}_{(2)}, X^{(0)}{}_{(3)}, \cdots X^{(0)}{}_{(n)} \right\} \tag{8}$$

The corresponding time sequence is

$$\{t\} = \{t_1, t_2, t_3, \cdots t_n\} \tag{9}$$

where $X^{(0)}$ represents the wet adhesion (nonnegative value), t is the immersion period, and n is the sample size of the data.

An accumulating generation operator (AGO), or inverse AGO, is the precondition of the establishment of the gray model, which can smooth randomness and strengthen the regularity of the sequence. Here, gray sequence generation is performed by AGO, and the monotonically increasing sequence $X^{(1)}$ is obtained as follows:

$$\left\{ X^{(1)} \right\} = \left\{ X^{(1)}{}_{(1)}, X^{(1)}{}_{(2)}, X^{(1)}{}_{(3)}, \cdots X^{(1)}{}_{(n)} \right\} \tag{10}$$

where

$$\left\{ X^{(1)}{}_{(k)} \right\} = \sum_{i=1}^{k} X^{(0)}{}_{(i)}, (k = 1, 2, 3 \cdots n). \tag{11}$$

The mean sequence $Z^{(1)}$ of $X^{(1)}$ is defined as follows:

$$\left\{ Z^{(1)} \right\} = \left\{ Z^{(1)}{}_{(1)}, Z^{(1)}{}_{(2)}, Z^{(1)}{}_{(3)}, \cdots Z^{(1)}{}_{(n)} \right\} \tag{12}$$

where

$$Z^{(1)}{}_{(k)} = \frac{1}{2} \left[X^{(1)}{}_{(k)} + X^{(1)}{}_{(k-1)} \right], (k = 2, 3, 4 \cdots n). \tag{13}$$

The least-square estimate sequence of the gray differential equation is as follows:

$$\partial Z^{(1)}{}_{(k)} + X^{(0)}{}_{(k)} = u. \tag{14}$$

Then, the GM (1, 1) whitening differential equation of $X^{(1)}{}_{(k)}$ is as follows:

$$\partial X^{(1)}{}_{(k)} + \frac{\mathrm{d} X^{(1)}{}_{(k)}}{\mathrm{d} t} = u. \tag{15}$$

where the parameters a and u can be determined by the least-square method:

$$[\partial, u]^T = \left(B^T B \right)^{-1} B^T \gamma_n \tag{16}$$

where

$$B = \begin{bmatrix} -Z^{(1)}{}_{(2)} & 1 \\ -Z^{(1)}{}_{(3)} & 1 \\ \vdots & \vdots \\ -Z^{(1)}{}_{(n)} & 1 \end{bmatrix} \tag{17}$$

$$Y_n = \left[X^{(0)}{}_{(2)}, X^{(0)}{}_{(3)}, X^{(0)}{}_{(4)}, \cdots X^{(0)}{}_{(n)} \right] \tag{18}$$

The solution of $X^{(1)}{}_{(k)}$ at time k is

$$X_p{}^{(1)}{}_{(k)} = \left[X^{(0)}{}_{(1)} - \frac{u}{\partial} \right] e^{-a(k-1)} + \frac{u}{\partial}, (k = 2, 3, 4 \cdots n). \tag{19}$$

As above, p represents the predicted value. Then, to obtain the predicted value of the primitive data at time k, the Inverse Accumulating Generation Operator (IAGO) is used to establish the following GM (1, 1):

$$X_p{}^{(0)}{}_{(k)} = \left[X^{(0)}{}_{(1)} - \frac{u}{\partial} \right] e^{-a(k-1)} + (1 - e^a), (k = 2, 3, 4 \cdots n). \tag{20}$$

For

$$t = t_1 + N(k - 1) \tag{21}$$

by replacing the parameter k with t, the following equation can be obtained:

$$X_p{}^{(0)}{}_{(k)} = \left[X^{(0)}{}_{(1)} - \frac{u}{\partial} \right] e^{-a\left(\frac{t - t_1}{N} \right)} (1 - e^a), (t \geq t_1 + N). \tag{22}$$

In the above equation, t_1 is the initial time of the time sequence, and N is the time interval of the arithmetic series. Equation (22) is the gray GM (1, 1) model of the coating based on GST for the wet adhesion of coatings. The measured adhesion data are calculated according to the above steps, and the resulting coefficients ∂ and u are summarized in Table 2 using the associated adhesion model.

Table 2. Parameters obtained from the calculations of the wet adhesion of coatings using the GM (1, 1) model.

Temp.	∂	u
20 °C	0.1142	16.8425
40 °C	0.1916	19.6115

The calculated parameters ∂ and u are substituted into Equation (22), and the equations for coating adhesion versus time at different temperatures can be obtained.

$$X_p^{(0)}{}_{(t)} = 15.85708e^{-0.1142t/48} \tag{23}$$

$$X_p^{(0)}{}_{(t)} = 18.15148e^{-0.1916t/48} \tag{24}$$

In order to analyze the accuracy of the GM (1, 1) model, the average relative error of the model is analyzed. The average relative error, ARE, is calculated using the following formula:

$$ARE = \frac{1}{n}\sum_{k=2}^{n} \frac{\left| X^{(0)}{}_{(k)} - X_p^{(0)}{}_{(k)} \right|}{X^{(0)}{}_{(k)}} \times 100\% \tag{25}$$

The average relative error of the GM (1, 1) model at 20 °C and 40 °C is 9.3% and 9.6%, respectively. It can be seen that the overall accuracy of the established GM (1, 1) model is good. The coating adhesion has a great influence on the aging behavior of the coating.

4.3. Coating Strength Evolution

For the tensile strength of the coating, the immersion time is taken as the independent variable and the strength value as the variable. After taking the natural logarithm of the longitudinal tensile strength, the soaking time is plotted, as shown in the figure below. After linear fitting, the fitting parameters were obtained, as shown in Table 3. Table 3 is the coefficient obtained after fitting the coating strength equation. It can be seen that the relationship between coating strength and soaking time is as follows:

$$\sigma = \frac{S}{e^{bt}} \tag{26}$$

As shown in Figure 10, the experimental curve matches the fitted curve well, and the fitting coefficients are summarized in Table 3.

Table 3. Coefficients obtained after fitting the coating strength equation.

Conditions	S	b
20 °C	55.147	1.02×10^{-4}
40 °C	54.598	8.77×10^{-4}

Then, the formula for the variation in the coating strength with time can be derived as follows:

$$\sigma^{20°C} = \frac{55.147}{e^{-1.02\times10^{-4}t}} \tag{27}$$

$$\sigma^{40°C} = \frac{54.598}{e^{-8.77\times10^{-4}t}} \tag{28}$$

From the analysis above, the tensile strength of the coating decreases at different temperatures, but its contribution to the aging behavior of the coating is limited. Especially when the temperature is low, the coating strength fluctuates greatly, but there is no obvious loss compared with other performance parameters in a short service time.
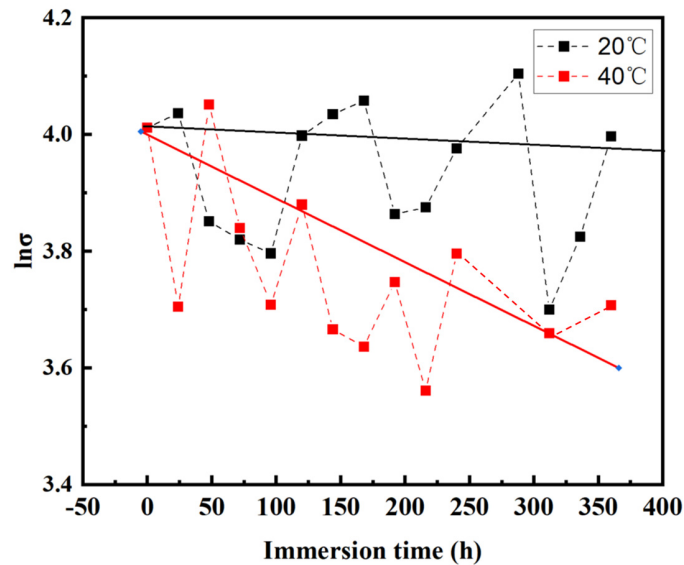
Figure 10. Variation in the strength of the electrophoretic coatings and the data fitting curve.

4.4. Coating Failure Behavior

The coating resistance curves as determined from the EIS fitting results are plotted as functions of immersion time in Figure 11 to investigate the coating failure behavior at different temperatures. The values of R_c gradually decrease, from approaching 10^{10} $\Omega \cdot cm^2$ to 6.97×10^7 $\Omega \cdot cm^2$ at 20 °C and to 1.64×10^7 $\Omega \cdot cm^2$ at 40 °C after 1 day. The rapid decrease of R_c in the initial stage of immersion suggests that water permeates into coatings quickly because of the relatively thin thickness of the coating. After 7 days, the impedance values of the coatings at 20 °C rapidly declined to their lowest point and then gradually stabilized. Analysis of the evolution of various coating properties indicates that the water absorption rate of the coating changed significantly during this period, consistent with the EIS analysis results. The adhesion of the coating initially decreased slowly but then started to decline more rapidly. This is attributed to the corrosion reaction occurring once water reached the alloy surface, which aligns with the SEM observation results. In contrast, the mechanical properties measured from the free film of the coating showed no significant changes, suggesting that these properties are likely not the primary cause of coating failure. The decline rate of R_c at 40 °C is higher than that of the coating at 20 °C, indicating that the aging of the coating is accelerated at higher temperatures. Regarding the observed temporary increase in R_c values after about 21 days, it can also be inferred from Figure 9 that the coating resistance increased due to the clogging of pores by corrosion products.
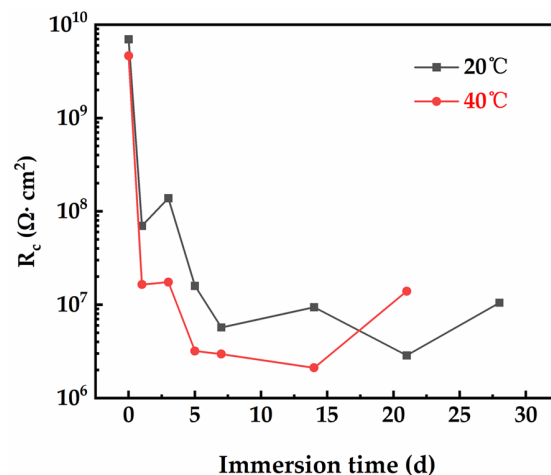

Figure 11. Coating resistance R_c as a function of the immersion time at 20 °C and 40 °C.

Based on the analysis above, organic electrophoretic coatings for magnesium alloys have potential automotive industry applications due to their excellent properties, such as uniform coating thickness, good adhesion, and corrosion resistance. In future work, the water transport, wet adhesion, and tensile strength failure models of electrophoretic coating are planned to be correlated during the failure process. By processing the data to evaluate the impact of these factors on coating failure, we aim to facilitate the prediction of the coating's service life, which can provide a theoretical basis for the maintenance and development of the coating.

5. Conclusions

In this study, a Nippon organic electrophoretic coating was selected as the coating material. The failure behavior and durability of the organic electrophoretic coatings were studied, which can provide some experimental guidance for failure analysis in practical automobile applications and even for the research of coating lifetime prediction. The water absorption kinetics, coating adhesion, and tensile strength of the coatings were studied after immersion in 3.5 wt.% NaCl at 20 °C and 40 °C. Furthermore, comparisons were made with the materials immersed at different temperatures. The main conclusions are as follows:

(1) Water absorption rates of the coating changed significantly during the initial stage, which is consistent with the EIS analysis results. The diffusion coefficient of the coating soaked at 40 °C is greater than that of the coating soaked at 20 °C. The water absorption of electrophoretic paint improved with increasing temperature.

(2) The gradually accumulating corrosion products and generated gases on the alloy surface pushed the coating until it cracked, leading to a decrease in coating adhesion. The gray GM (1, 1) model can be used to fit the trend of wet adhesion of the coating under immersion. The overall accuracy of the established GM (1, 1) model is good.

(3) The tensile strength of the coating does not change significantly with soaking time, and the contribution to the aging of the coating is less than that of coating adhesion and water diffusion.

Institutional Review Board Statement: Not applicable.

Informed Consent Statement: Not applicable.

Data Availability Statement: Data are contained within this article.

Conflicts of Interest: Xiaoxue Wang, Xiuchun Liu and Kai Gao were employed by the Beijing Institute of Space Long March Vehicle. The remaining authors declare that the research was conducted in the absence of any commercial or financial relationships that could be construed as potential conflicts of interest. The authors declare no conflicts of interest.

References

1. Prasad, S.V.S.; Prasad, S.B.; Verma, K.; Mishra, R.K.; Kumar, V.; Singh, S. The role and significance of Magnesium in modern day research-A review. *J. Magnes. Alloys* **2022**, *10*, 1–61. [CrossRef]
2. Trang, T.T.T.; Zhang, J.H.; Kim, J.H.; Zargaran, A.; Hwang, J.H.; Suh, B.C.; Kim, N.J. Designing a magnesium alloy with high strength and high formability. *Nat. Commun.* **2018**, *9*, 2522. [CrossRef]
3. Joost, W.J.; Krajewski, P.E. Towards magnesium alloys for high-volume automotive applications. *Scr. Mater.* **2017**, *128*, 107–112. [CrossRef]

4. Luo, A.A. Recent magnesium alloy development for automotive powertrain applications. In *Magnesium Alloys 2003, Pts 1 and 2*; Kojima, Y., Aizawa, T., Higashi, K., Kamado, S., Eds.; Trans Tech Publications, Ltd.: Stafa-Zurich, Switzerland, 2003; Volum 419–424, pp. 57–65.

5. Kulekci, M.K. Magnesium and its alloys applications in automotive industry. *Int. J. Adv. Manuf. Technol.* **2008**, *39*, 851–865. [CrossRef]

6. Wang, X.X.; Guo, J.J.; Zeng, Z.H.; Zhou, P.; Wang, R.Q.; Liu, X.C.; Gao, K.; Sun, J.L.; Yuan, Y.; Wang, F.H. A Semi-Mechanistic Model for Predicting the Service Life of Composite Coatings on VW63Z Magnesium Alloy. *Acta Metall. Sin.-Engl. Lett.* **2024**, *37*, 1161–1176. [CrossRef]

7. Liu, W.C.; Wen, L.; Meng, D.H.; Pang, S.; Xiao, L.; Zhou, B.P.; Wu, G.H. High-Cycle Fatigue Behavior of Deep Cryogenic-Elevated Temperature Cycling Treated Sand-Cast Mg-6Gd-3Y-0.5Zr Alloy. *Adv. Eng. Mater.* **2021**, *23*, 2100234. [CrossRef]

8. Xu, T.C.; Yang, Y.; Peng, X.D.; Song, J.F.; Pan, F.S. Overview of advancement and development trend on magnesium alloy. *J. Magnes. Alloys* **2019**, *7*, 536–544. [CrossRef]

9. Esmaily, M.; Svensson, J.E.; Fajardo, S.; Birbilis, N.; Frankel, G.S.; Virtanen, S.; Arrabal, R.; Thomas, S.; Johansson, L.G. Fundamentals and advances in magnesium alloy corrosion. *Prog. Mater. Sci.* **2017**, *89*, 92–193. [CrossRef]

10. Agarwal, S.; Curtin, J.; Duffy, B.; Jaiswal, S. Biodegradable magnesium alloys for orthopaedic applications: A review on corrosion, biocompatibility and surface modifications. *Mater. Sci. Eng. C Mater. Biol. Appl.* **2016**, *68*, 948–963. [CrossRef]

11. Li, H.T.; Si, S.H.; Yang, K.; Mao, Z.A.; Sun, Y.H.; Cao, X.R.; Yu, H.T.; Zhang, J.W.; Ding, C.; Liang, H.X.; et al. Hexafluoroisopropanol based silk fibroin coatings on AZ31 biometals with enhanced adhesion, corrosion resistance and biocompatibility. *Prog. Org. Coat.* **2023**, *184*, 107881. [CrossRef]

12. Singh, N.; Batra, U.; Kumar, K.; Ahuja, N.; Mahapatro, A. Progress in bioactive surface coatings on biodegradable Mg alloys: A critical review towards clinical translation. *Bioact. Mater.* **2023**, *19*, 717–757. [CrossRef]

13. Kaseem, M.; Fatimah, S.; Nashrah, N.; Ko, Y.G. Recent progress in surface modification of metals coated by plasma electrolytic oxidation: Principle, structure, and performance. *Prog. Mater. Sci.* **2021**, *117*, 100735. [CrossRef]

14. Darband, G.B.; Aliofkhazraei, M.; Hamghalam, P.; Valizade, N. Plasma electrolytic oxidation of magnesium and its alloys: Mechanism, properties and applications. *J. Magnes. Alloys* **2017**, *5*, 74–132. [CrossRef]

15. Telmenbayar, L.; Ramu, A.G.; Yang, D.; Choi, D. Development of mechanically robust and anticorrosion slippery PEO coating with metal-organic framework (MOF) of magnesium alloy. *Chem. Eng. J.* **2023**, *458*, 141397. [CrossRef]

16. Gnedenkov, A.S.; Sinebryukhov, S.L.; Filonina, V.S.; Ustinov, A.Y.; Sukhoverkhov, S.V.; Gnedenkov, S.V. New Polycaprolactone-Containing Self-Healing Coating Design for Enhance Corrosion Resistance of the Magnesium and Its Alloys. *Polymers* **2022**, *15*, 202. [CrossRef]

17. Bai, Y.; Yu, F.L.; Du, J.; Wang, W.X.; Cui, Z.Q.; Han, Z.H.; Yang, J.F. A Brief Review about Surface Treatment of Magnesium Alloys. In Proceedings of the 13th International Symposium on Eco-Materials Processing and Design (ISEPD 2012), Guilin, China, 7–10 January 2012; pp. 307–310.

18. Chen, X.M.; Li, G.Y.; Lian, J.S.; Jiang, Q. An organic chromium-free conversion coating on AZ91D magnesium alloy. *Appl. Surf. Sci.* **2008**, *255*, 2322–2328. [CrossRef]

19. Galio, A.F.; Lamaka, S.V.; Zheludkevich, M.L.; Dick, L.F.; Mueller, I.L.; Ferreira, M.G.S. Evaluation of Corrosion Protection of Sol-Gel Coatings on AZ31B Magnesium Alloy. In Proceedings of the 13th Conference of the Sociedade-Portuguesa-de-Materiais/4th International Materials Symposium, Oporto, Portugal, 1–4 April 2007; pp. 390–394.

20. Zhang, D.X.; Xiang, Q.; Li, X.M. Electrophoretic fabrication of zeolitic imidazolate framework-67 (ZIF-67) and its derivative coating. *Mater. Lett.* **2019**, *257*, 126686. [CrossRef]

21. Estupinan Lopez, F.H.; Gaona Tiburcio, C.; Baltazar-Zamora, M.A.; Sepulveda, S.; Zambrano Robledo, P.; Cabral Miramontes, J.A.; Almeraya Calderon, F. Effect of the Addition of Nanoparticles in the Mechanical and Electrochemical Behavior of Electrophoretic Coatings. In Proceedings of the 32nd National Congress of the Mexican-Electrochemical-Society (MES)/10th Meeting of the Mexican-Section of the Electrochemical-Society (ECS), Guanajuato, Mexico, 5–8 June 2017; pp. 279–290.

22. Yao, W.M.; Wang, Z.P.; Wu, X.; Li, B.B.; Zhong, X.M.; Lin, J.; Chen, J.Y.; Lai, Y.H. Preparation of coatings from a series of silicone/fluorine-functionalized polyacrylates via electrophoretic deposition. *Polym. Adv. Technol.* **2015**, *26*, 1148–1154. [CrossRef]

23. Stoch, A.; Brozek, A.; Kmita, G.; Stoch, J.; Jastrzebski, W.; Rakowska, A. Electrophoretic coating of hydroxyapatite on titanium implants. *J. Mol. Struct.* **2001**, *596*, 191–200. [CrossRef]

24. Atrens, A.; Song, G.L.; Liu, M.; Shi, Z.M.; Cao, F.Y.; Dargusch, M.S. Review of Recent Developments in the Field of Magnesium Corrosion. *Adv. Eng. Mater.* **2015**, *17*, 400–453. [CrossRef]

25. Van Phuong, N.; Moon, S. Deposition and characterization of E-paint on magnesium alloys. *Prog. Org. Coat.* **2015**, *89*, 91–99. [CrossRef]

26. Li, X.J.; Shi, H.; Cui, Y.; Pan, K.; Wei, W.; Liu, X.Y. Dextran-caffeic acid/tetraaniline composite coatings for simultaneous improvement of cytocompatibility and corrosion resistance of magnesium alloy. *Prog. Org. Coat.* **2020**, *149*, 105928. [CrossRef]

27. Lin, J.; Nguyen, N.T.; Zhang, C.; Ha, A.; Liu, H.H. Antimicrobial Properties of MgO Nanostructures on Magnesium Substrates. *ACS Omega* **2020**, *5*, 24613–24627. [CrossRef] [PubMed]

28. Maqsood, M.F.; Raza, M.A.; Ghauri, F.A.; Rehman, Z.U.; Ilyas, M.T. Corrosion study of graphene oxide coatings on AZ31B magnesium alloy. *J. Coat. Technol. Res.* **2020**, *17*, 1321–1329. [CrossRef]

29. Wang, Z.X.; Xu, L.; Zhang, J.W.; Ye, F.; Lv, W.G.; Xu, C.; Lu, S.; Yang, J. Preparation and Degradation Behavior of Composite Bio-Coating on ZK60 Magnesium Alloy Using Combined Micro-Arc Oxidation and Electrophoresis Deposition. *Front. Mater.* **2020**, *7*, 190. [CrossRef]

30. Wu, M.; Guo, Y.H.; Xu, G.L.; Cui, Y.W. Effects of Deposition Thickness on Electrochemical Behaviors of AZ31B Magnesium Alloy with Composite Coatings Prepared by Micro-arc Oxidation and Electrophoretic Deposition. *Int. J. Electrochem. Sci.* **2020**, *15*, 1378–1390. [CrossRef]

31. Liu, X.L.; Feng, T.; Meng, X.Y.; Wen, S.F.; Hou, W.B.; Ding, J.H.; Lin, H.J.; Yue, Z.F. Effect of SiC nanowires on adhesion and wear resistance of hydroxyapatite coating on AZ31 magnesium alloy. *J. Alloys Compd.* **2023**, *960*, 170934. [CrossRef]

32. Jafari, Z.; Pishbin, F.; Ghambari, M.; Dehghanian, C. Surface modification of AZ31 Mg alloy by diopside/fluorohydroxyapatite/graphene oxide nanocomposite coating: Corrosion and bioactivity evaluations. *J. Alloys Compd.* **2024**, *976*, 172961. [CrossRef]

33. Liu, X.; Ding, J.; Hou, W.; Shi, X.; Feng, T.; Meng, X.; Wen, S.; Tong, M.; Yue, Z. Microstructural, mechanical and corrosion characterization of (C-HA)SiCnws coating on AZ31 magnesium alloy surface. *Surf. Coat. Technol.* **2024**, *476*. [CrossRef]

34. Yang, J.; Dong, K.; Song, Y.; Cheng, X.; Dong, Q.; Han, E.-H. Deposition mechanism of cathodic electrophoresis coating on Mg alloys: Effects of Mg substrates on deposition process. *Prog. Org. Coat.* **2024**, *187*, 130207. [CrossRef]

35. Zhang, R.; Liang, J.; Wang, Q. Preparation and characterization of graphite-dispersed styrene-acrylic emulsion composite coating on magnesium alloy. *Appl. Surf. Sci.* **2012**, *258*, 4360–4364. [CrossRef]

36. Wu, L.; Ding, X.; Zheng, Z.; Ma, Y.; Atrens, A.; Chen, X.; Xie, Z.; Sun, D.; Pan, F. Fabrication and characterization of an actively protective Mg-Al LDHs/Al2O3 composite coating on magnesium alloy AZ31. *Appl. Surf. Sci.* **2019**, *487*, 558–568. [CrossRef]

37. Singh, S.; Singh, G.; Bala, N. Synthesis and characterization of iron oxide-hydroxyapatite-chitosan composite coating and its biological assessment for biomedical applications. *Prog. Org. Coat.* **2021**, *150*, 106011. [CrossRef]

38. Rojaee, R.; Fathi, M.; Raeissi, K.; Sharifnabi, A. Biodegradation assessment of nanostructured fluoridated hydroxyapatite coatings on biomedical grade magnesium alloy. *Ceram. Int.* **2014**, *40 Pt B*, 15149–15158. [CrossRef]

39. Sun, J.; Zhu, Y.; Meng, L.; Chen, P.; Shi, T.; Liu, X.; Zheng, Y. Electrophoretic deposition of colloidal particles on Mg with cytocompatibility, antibacterial performance, and corrosion resistance. *Acta Biomater.* **2016**, *45*, 387–398. [CrossRef] [PubMed]

40. Askarnia, R.; Ghasemi, B.; Fardi, S.R.; Adabifiroozjaei, E. Improvement of tribological, mechanical and chemical properties of Mg alloy (AZ91D) by electrophoretic deposition of alumina/GO coating. *Surf. Coat. Technol.* **2020**, *403*, 126410. [CrossRef]

41. Gnedenkov, S.V.; Sinebryukhov, S.L.; Mashtalyar, D.V.; Imshinetskiy, I.M. Composite fluoropolymer coatings on Mg alloys formed by plasma electrolytic oxidation in combination with electrophoretic deposition. *Surf. Coat. Technol.* **2015**, *283*, 347–352. [CrossRef]

42. Lee, W.S.; Park, M.; Kim, M.H.; Park, C.G.; Huh, B.K.; Seok, H.K.; Choy, Y.B. Nanoparticle coating on the silane-modified surface of magnesium for local drug delivery and controlled corrosion. *J. Biomater. Appl.* **2016**, *30*, 651–661. [CrossRef] [PubMed]

43. Liu, L.; Peng, F.; Zhang, D.; Li, M.; Huang, J.; Liu, X. A tightly bonded reduced graphene oxide coating on magnesium alloy with photothermal effect for tumor therapy. *J. Magnes. Alloys* **2022**, *10*, 3031–3040. [CrossRef]

44. Gnedenkov, A.S.; Lamaka, S.V.; Sinebryukhov, S.L.; Mashtalyar, D.V.; Egorkin, V.S.; Imshinetskiy, I.M.; Zheludkevich, M.L.; Gnedenkov, S.V. Control of the Mg alloy biodegradation via PEO and polymer-containing coatings. *Corros. Sci.* **2021**, *182*, 109254. [CrossRef]

45. Saji, V.S. Electrophoretic (EPD) coatings for magnesium alloys. *J. Ind. Eng. Chem.* **2021**, *103*, 358–372. [CrossRef]

46. Tayyaba, Q.; Shahzad, M.; Butt, A.Q.; Rafi-ud-din; Khan, M.; Qureshi, A.H. The influence of electrophoretic deposition of HA on Mg-Zn-Zr alloy on its in-vitro degradation behaviour in the Ringer's solution. *Surf. Coat. Technol.* **2019**, *375*, 197–204. [CrossRef]

47. Hu, D.; Lv, Z.; Liu, H.; Jing, F.; Zhao, Y.; Zhang, S.; Du, H.; Wang, R. Characterization and mechanical modeling of interfacial damage in EB-PVD thermal barrier coatings considering multiple failure factors. *J. Mater. Sci. Technol.* **2024**, *190*, 42–55. [CrossRef]

48. da Silva Lopes, T.; Lopes, T.; Martins, D.; Carneiro, C.; Machado, J.; Mendes, A. Accelerated aging of anticorrosive coatings: Two-stage approach to the AC/DC/AC electrochemical method. *Prog. Org. Coat.* **2020**, *138*, 105365. [CrossRef]

49. Kamisho, T.; Takeshita, Y.; Sakata, S.; Sawada, T. Water absorption of water-based anticorrosive coatings and its effect on mechanical property and adhesive performance. *J. Coat. Technol. Res.* **2014**, *11*, 199–205. [CrossRef]

50. Zhang, C.; Bao, X.; Li, W.; Chen, L.; Du, M. Effect of temperature on Brillouin gain spectrum and aging behavior in carbon/polyimide coated fiber. In Proceedings of the 19th International Conference on Optical Fibre Sensors, Perth, Australia, 15–18 April 2008.

51. Fang, B.Y.; Han, E.H.; Wang, J.Q.; Zhu, Z.Y.; Ke, W.; Hu, J.P.; Xu, Z.A. Effect of aging temperature and time on the performance of epoxy coating. *Acta Metall. Sin.* **2003**, *39*, 533–540.

52. Guermazi, N.; Elleuch, K.; Ayedi, H.F. The effect of time and aging temperature on structural and mechanical properties of pipeline coating. *Mater. Des.* **2009**, *30*, 2006–2010. [CrossRef]

53. Lopez-Ortega, A.; Bayon, R.; Arana, J.L. Evaluation of Protective Coatings for High-Corrosivity Category Atmospheres in Offshore Applications. *Materials* **2019**, *12*, 1325. [CrossRef] [PubMed]

54. Gharbi, O.; Tran, M.T.T.; Tribollet, B.; Turmine, M.; Vivier, V. Revisiting cyclic voltammetry and electrochemical impedance spectroscopy analysis for capacitance measurements. *Electrochim. Acta* **2020**, *343*, 136109. [CrossRef]

55. Gnedenkov, A.S.; Filonina, V.S.; Sinebryukhov, S.L.; Gnedenkov, S.V. A Superior Corrosion Protection of Mg Alloy via Smart Nontoxic Hybrid Inhibitor-Containing Coatings. *Molecules* **2023**, *28*, 2538. [CrossRef]

56. Yang, C.; Cui, S.; Fu, R.K.Y.; Sheng, L.; Wen, M.; Xu, D.; Zhao, Y.; Zheng, Y.; Chu, P.K.; Wu, Z. Optimization of the in vitro biodegradability, cytocompatibility, and wear resistance of the AZ31B alloy by micro-arc oxidation coatings doped with zinc phosphate. *J. Mater. Sci. Technol.* **2024**, *179*, 224–239. [CrossRef]

57. Meng, F.D.; Liu, L.; Tian, W.L.; Wu, H.; Li, Y.; Zhang, T.; Wang, F.H. The influence of the chemically bonded interface between fillers and binder on the failure behaviour of an epoxy coating under marine alternating hydrostatic pressure. *Corros. Sci.* **2015**, *101*, 139–154. [CrossRef]

58. Meng, F.D.; Liu, L.; Liu, E.H.; Zheng, H.P.; Liu, R.; Cui, Y.; Wang, F.H. Synergistic effects of fluid flow and hydrostatic pressure on the degradation of epoxy coating in the simulated deep-sea environment. *Prog. Org. Coat.* **2021**, *159*, 106449. [CrossRef]

59. Meng, F.D.; Liu, Y.; Liu, L.; Li, Y.; Wang, F.H. Studies on Mathematical Models of Wet Adhesion and Lifetime Prediction of Organic Coating/Steel by Grey System Theory. *Materials* **2017**, *10*, 715. [CrossRef]

60. Deng, J.L. Control problems of grey systems. *Syst. Control Lett.* **1982**, *1*, 288–294.